Spatial-temporal turbulent flow-field and heat transfer behavior in end-wall junctions

T. J. Praisner, C. V. Seal, L. Takmaz, and C. R. Smith
Department of Mechanical Engineering and Mechanics, Lehigh University, Bethlehem, PA

The spatial-temporal velocity and surface heat transfer behavior in a rectangular end-wall junction are examined experimentally for an impinging turbulent boundary layer. The study is done in a water channel on a fast response, constant heat-flux surface using flow visualization, scanned-laser particle image velociemtry (PIV), and thermochromic liquid crystals (LC). Particle image visualizations and PIV-derived vorticity isocontours in the junction region of a rectangular block illustrate that a dominant unsteady horseshoe vortex resides in the junction region, as suggested by previous studies[2] (Devenport and Simpson 1990; Pierce and Shin 1992). The horseshoe vortex moves sporadically within a spatial envelope, due to the interaction with both (1) vortices from the impinging turbulent boundary layer; and (2) intermittent, opposite rotation vortices spawned by eruptive vortex–surface interactions (Walker 1978; Peridier et al. 1991). Companion surface heat transfer studies using thermochromic liquid crystals of both a canonical turbulent boundary layer and the rectangular block junction illustrate the presence of initially discrete spanwise variations in heat transfer on the approach surface caused by the presence of the streamwise, near-wall "streaks" in the impinging turbulent boundary layer; in the junction region, these streaks undergo a rapid metamorphosis into discrete, transverse regions of high heat transfer. These localized regions display significant transient, three-dimensional (3-D) behavior, appearing to be directly associated with vortex–surface interactions by the resident horseshoe vortex. This milieu of turbulent vortex development/interaction results in increases of 62% in spatially averaged Stanton number and increases of over 200% in local Stanton number compared to the canonical turbulent boundary layer. *© 1997 by Elsevier Science Inc.*

Keywords: heat transfer behavior; spatial-temporal velocity; turbulent flow-field

Introduction

When a bluff body obstruction is located on a surface with an impinging turbulent boundary layer, the strong adverse pressure gradient imposed on the approaching flow causes the boundary layer to separate, precipitating the formation of a "horseshoe vortex", with legs that circumscribe the leading-edge region of the bluff body and tail downstream (Devenport and Simpson 1990; Pierce and Shin 1992), as shown in Figure 1. This horseshoe vortex dominates the flow in the junction region between the approach surface and the bluff body and is characterized by significant aperiodic unsteadiness, with the adjacent wall region characterized by highly elevated levels of surface heat transfer (Lewis et al. 1994). Such turbulent juncture flows characterize many practical flows; among them, wing–fuselage junctions on aircraft, conning tower–body junctions on submarines, turbomachinery blade–rotor junctions, and even electronic cooling devices.

The mean flow field for a turbulent wing–body junction has been well documented in a number of studies (Kays and Crawford 1980), including mean spatial velocity and pressure fields, probability distributions, and rms properties. The conclusion from these studies is that the velocity field is quite unsteady, displaying double-peaked velocity and surface pressure probability distributions indicative of apparent spatial–temporal changes in the position of the horseshoe vortex, thought to be attributable to unsteady stretching effects and interaction of the horseshoe vortex with newly generated surface vortices (Devenport and Simpson 1990). The impact of the horseshoe vortex on surface heat transfer has been shown by Lewis et al. (1994), using arrays of surface heat transfer gauges, to be quite significant, with increases in junction-region heat transfer of up to 200% above conventional flat-plate values and rms variations of up to 25% of the local mean values. Ireland and Jones (1986) found mean profiles of elevated heat transfer suggesting the same behavior as that found by Lewis et al. However, the physical relationship between the junction-region fluid dynamics and surface heat flux, particularly the relationship between the junction horseshoe vortex and local, temporal heat flux behavior has not been clearly established.

In seminal numerical studies of Walker (1978), Ersoy and Walker (1995), Peridier et al. (1991), and Puhak et al. (1993), the

---

Address reprint requests to Dr. C. R. Smith, Department of Mechanical Engineering and Mechanics; Lehigh University, 19 Memorial Drive West, Bethlehem, PA 18015, USA.

Received 10 March 1996; accepted 15 October 1996

Int. J. Heat and Fluid Flow 18: 142–151, 1997

655 Avenue of the Americas, New York, NY 10010

0142-727X/97/$17.00
PII S0142-727X(96)00141-0

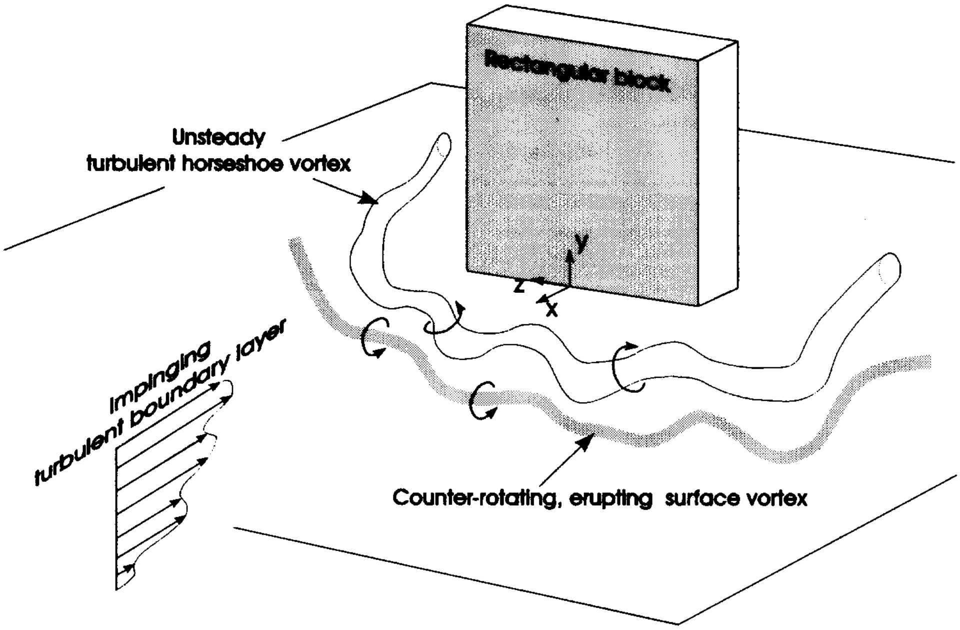

Figure 1 Schematic of the turbulent horseshoe vortex system

interaction of vortices in close proximity to surfaces has been shown to have a significant effect on both flow behavior and surface heat transfer. In the most comprehensive study of flow behavior, Peridier et al. employed a Lagrangian numerical approach to simulate the flow induced by a single vortex above an infinite plate. These results show that as a primary vortex approaches a surface, it stimulates the development of the local boundary layer (due to the vortex-imposed surface pressure gradient), which rapidly focuses into a region of unsteady separation, manifested by the appearance of a closed, recirculating eddy, or secondary vortex, within the boundary layer. Depending upon the strength and proximity of the primary vortex, this generated eddy grows rapidly, with a strong upflow induced between the primary and secondary vortices. Ultimately, the secondary vortex is ejected into the outer flow, in conjunction with a narrow eruption of the boundary layer, which interacts strongly with the outer flow. An illustration of this temporal separation process is shown schematically in Figure 2.

Puhak et al. (1993) studied the development of an unsteady boundary-layer flow for an impulsively started flow upstream of a circular-cylinder, end-wall junction with uniform surface heating. Their numerical calculations on the streamwise symmetry plane suggest the development of a three-dimensional (3-D) separation upstream of the cylinder, which results in a marked local *decrease* in surface heat transfer in proximity to the flow separation. Immediately downstream of this sharp decrease, the heat transfer rate increases as the leading edge of the cylinder is approached. At this stage, the physical interpretation of such boundary-layer separation on unsteady surface heat transfer is not clearly understood and has not been observed experimentally.

Several studies of junction flows with *laminar* approach boundary layers have illustrated the development of multiple "necklace" vortices in the junction region, which behave in a steady or unsteady periodic manner, depending upon the geometry and Reynolds number (Seal et al. 1995). Using these orga-

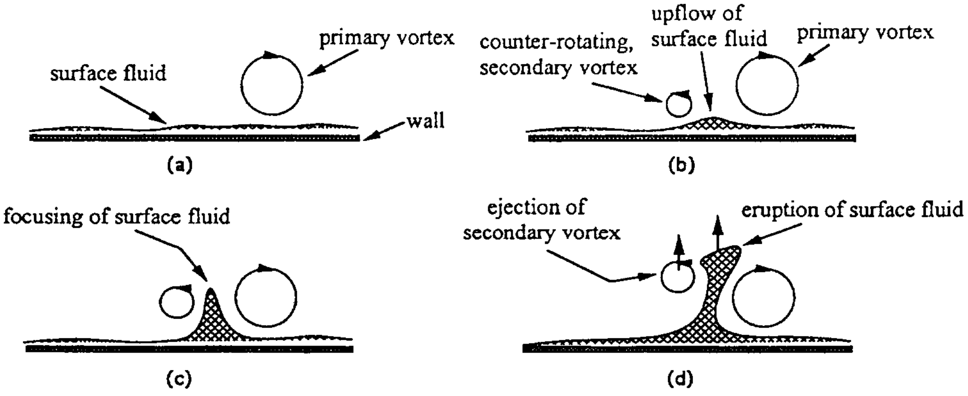

Figure 2 Schematic illustrating process of vortex–surface interaction and eruption of surface fluid (after Peridier et al. 1991)

nized, repetitive vortex flow structures as an experimental test environment, Seal et al. employed particle image velocimetry (PIV) to examine experimentally the behavior of the vorticity field and the vortex–surface interaction process for a selected periodic flow in which the necklace vortices form periodically and translate toward a rectangular bluff body. Figure 3 is a short sequence from Seal et al. illustrating the behavior of the temporal vorticity field during the formation, translation, and amalgamation of the necklace vortices. As revealed by this sequence, positive vorticity concentrates into the necklace vortices from impinging boundary-layer vorticity, translates toward the block, and ultimately amalgamates with a resident corner vortex. In Figure 3, note that as the necklace vortex translates toward the block, the type of vortex–surface interaction predicted by Peridier et al. (1991) occurs, causing low-momentum near-wall fluid of negative vorticity to be ejected outward in the upwash region of the vortex (to the left of all distinct vortices).

It is clear that elevation of surface heat transfer in turbulent wall-junction regions is associated with the development and behavior of a dominant, unsteady horseshoe-type vortex. In addition, recent laminar studies suggest that the interaction of wall-region vortices with surface fluid creates strongly eruptive behavior that seems to be at least partially responsible for the generation of observed unsteady flow behavior. However, the details of the vortex interaction processes in a turbulent junction flow are poorly understood, and the consequent relationship to instantaneous variations of surface heat transfer is still speculative. Thus, it is the objective of the present paper to provide details on spatial–temporal flow behavior and surface heat transfer in the junction region of a bluff body with a turbulent approach flow and to provide a physical interpretation of the results in terms of vortex–surface interactions. We report on an initial study using a rectangular junction body with a single, low-Reynolds number turbulent approach flow.

Experimental apparatus and procedure

A free-surface, closed-loop water channel described and validated previously by Seal et al. (1995) was used for all studies. As shown in Figure 4, the main test plate was a 1.9-cm Plexiglas plate, 200-cm long × 88-cm wide with a 5:1 elliptical leading edge. A rectangular Plexigals block (20-cm high × 15.2-cm wide × 5.1-cm deep), located 135 cm from the leading edge, created a junction region on the main test plate. A free-stream velocity of 10 cm/s was employed, which gave a Reynolds number based on distance from the leading edge of 1.5×10^5 at the block junction. To ensure a uniform impinging turbulent boundary layer, the boundary layer was tripped 6 cm from the leading edge of the flat plate using a threaded 0.6-cm rod; the Reynolds number based on the flat-plate displacement thickness (i.e., Re_θ) at the *equivalent* point of the block junction (i.e., without the block present) was 600, which classifies the flow as a minimal turbulent boundary layer. The thermal boundary layer was initiated 104 cm from the leading edge using a constant heat flux insert.

The body of the constant heat flux insert was machined from Plexiglas and mounted in the main test plate, as shown in Figure 4. Four threaded-rod supports allowed the heat flux insert to be aligned flush with the main test plate surface. The active surface of the heat flux insert is a 51-μm thick stainless steel foil stretched over a centrally located cavity in the insert, 27.9-cm wide × 48.3-cm long × 0.32-cm deep, as shown in Figure 4. The foil wraps around the circular streamwise ends of the insert and

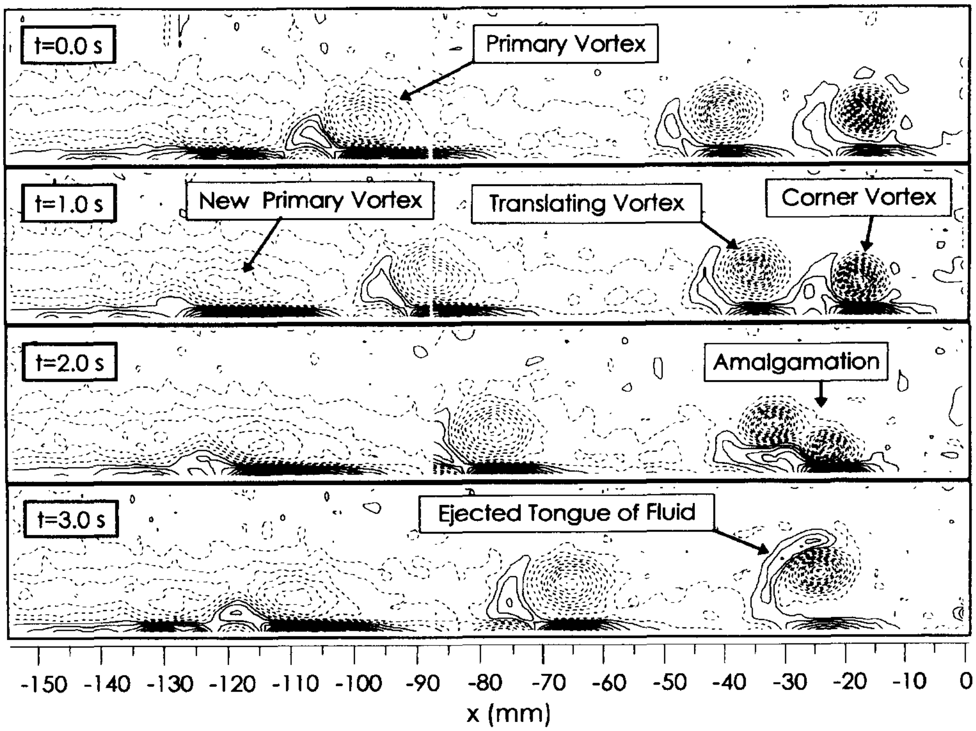

Figure 3 Sequential spatial-temporal vorticity contours on the symmetry plane for a laminar boundary layer impinging on a rectangular bluff body; flow left to right, with block at right edge; dashed lines indicate positive vorticity; solid lines indicate negative vorticity (after Seal at al. 1995)

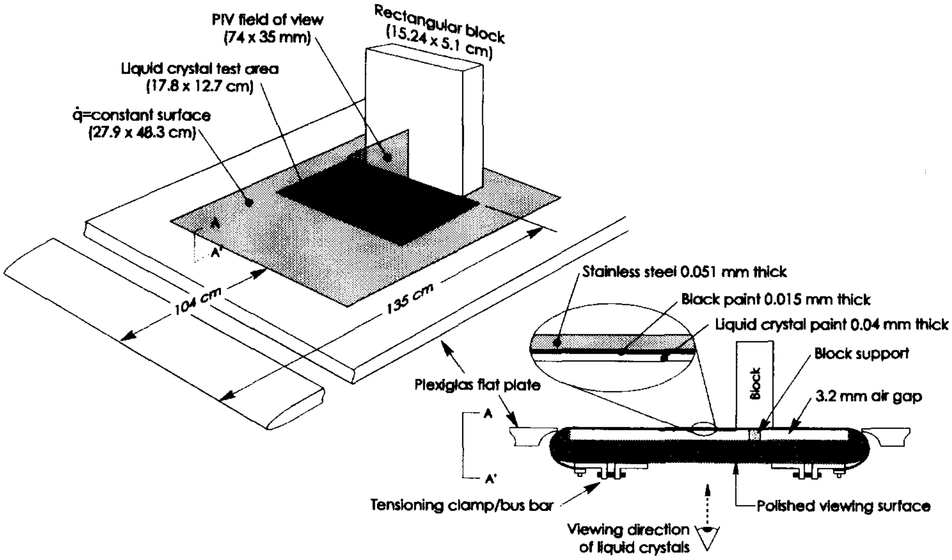

Figure 4 Schematic of experimental configuration and heat transfer section

is placed under uniform tension using specially designed tensioning clamps, which also function as bus bars for galvanic heating of the foil. The stretched foil overlaps the cavity laterally by 0.25 cm; silicone grease applied between the edges of the foil and the Plexiglas surface provide a watertight seal, leaving the cavity free from water exposure. Pressure equalization taps connected to a self-pressurizing tubing arrangement keep their air cavity beneath the foil in pressure equilibrium when the test section is submerged.

A constant heat flux condition is generated by galvanically heating the foil using an adjustable low-voltage (< 6V) ac power supply (a variable transformer and two step-down transformers connected in parallel), connected through the foil clamp/bus bars at each streamwise end of the foil. The use of low-voltage and high-amperage power is dictated by safety considerations and the low-resistance characteristics of the heater foil. Detailed tests of the active foil surface indicate spanwise voltage variations of less than 0.7%, and thus very uniform galvanic heat generation. Calibration of the foil heating surface was done by monitoring voltage and corresponding current flow across the extent of the heating foil, indicating a range of constant heat flux from 94 W/m^2 at 12% variac setting of 15,000 W/m^2 at 80% variac setting.

To provide surface temperature visualization, the cavity side of the heating foil side is coated first with a 15-μm layer of blank ink, then a 40-μm layer of temperature-sensitive liquid crystals (LC) in a water-based slurry using an air-brush applicator. The thermochromic liquid crystals employed in the present study are R25C5W-S40 chiral nematic liquid crystals from Hallcrest manufacturing, which have an active color bandwidth of 5 C, showing red color at 25 C and blue color at 30 C; a change in color of the liquid crystals under a constant heat flux corresponds directly to a local change in the foil surface temperature, and thus a variation in the local surface heat transfer coefficient. A numerical model of the transient behavior of the liquid crystal heating surface, assuming a step-change in the external surface temperature, indicates a 99% response in less than 0.1 second.

The liquid crystal-coated foil heat transfer surface was photographed directly using a 35-mm camera mounted below the water channel. To provide effective optical access, the bottom surface of the machined cavity in the heat flux insert was carefully polished. The rectangular body under examination was placed directly on the heat flux test section; a 1-cm × 4-cm × 0.32-cm thick block mounted in the cavity directly below the block ensured that the weight of the block would not deflect the foil surface.

Flow visualization techniques

Hydrogen bubble flow visualization and particle visualization techniques were employed to visualize the unsteady flow field. General flow-field behavior was investigated using a sheet of hydrogen bubbles generated from a transverse 25-μm diameter platinum wire, as described in Seal et al. (1995). Particle visualization was used for detailed visualization of the necklace vortex/surface interactions on the streamwise symmetry plane of the block. Particle visualization was done using laser sheet illumination of a suspension of spherical metallic-coated particles having a mean diameter of 12 μm and seeding concentration of about 2000 particles/cm^3. The light sheet was generated using a rotating, 72-facet mirror with variable frequency speed control, an optical focusing assembly, and a LEXEL 10-W argon–ion laser, as described in Seal et al. The laser sheet projected vertically, reflected off a mirror located downstream in the channel, and passed through the transparent rectangular block on the streamwise symmetry plane, as shown in Figure 4. The illuminated particles were viewed transverse to the flow direction using a three-chip, 720-line resolution color video camera and recorded on a high-performance video recorder for slow motion review. The characteristics of the observed particle motion were controlled by adjustment of the rotational speed of the mirror, which scanned the laser beam over a fixed region, repetitively illuminating the particles.

Particle image velocimetry measurements

High image-density particle image velocimetry (Adrian 1991; Rockwell et al. 1993) was used to investigate the velocity field on the symmetry plane of the rectangular block. The present study utilized the scanning laser system described above to illuminate the flow field. A 30-second sequence of 60 particle images was recorded at 0.5-s intervals using a motor-driven Nikon F4 35-mm camera with a bias mirror to correct for directional ambiguity. The images were analyzed on a PC-based interrogation system, which yields a field of two-dimensional (2-D) velocity vectors (see Seal et al. 1995 for details). To achieve sufficient spatial resolution, it was necessary to magnify the flow field, thus allowing a view of only a portion of the vortex system at one time. The field of view (74 mm × 35 mm) focused on the interaction region for the horseshoe vortex with the vortex located somewhat centrally in the field of view. The final results of the PIV experiments were a sequence of 60 velocity fields with a resolution of about 1.0 mm between vectors in the physical plane. These velocity datasets were then used to calculate vorticity using a Stokes theorem approach (Seal et al.). The spatial mean velocity field was approximated by temporally averaging the results from 60 sequential velocity fields; subtraction of the mean field from each instantaneous datafield allowed examination of the local Reynolds stress field, as well as other fluctuating properties.

Temperature visualization/quantification

Color image acquisition of spatial–temporal temperature patterns, and ultimately heat transfer coefficients, was done using photographic color slide images taken at 5.7 fps using a motor-driven Nikon F4. Each slide was then scanned into a Pentium PC using a Nikon Coolscan system as a 24-bit, 600 × 400 pixel RGB digital image, which was converted at HSI (Hue/Saturation/Intensity) format using Photostyler image-processing software. Conversion of the images to an HSI representation allows a more straightforward image-processing approach, because hue is the color attribute defining a pure color in HSI space and the color property that directly relates to the temperature of the thermochromic liquid crystals. To determine the respective surface temperature from the liquid crystal images, the hue component of each image was separated out as an 8-bit digital pixel array using the Photostyler software and calibrated using a temperature–hue calibration curve to establish the temperature distribution over the flow region.

The calibration curve was obtained in situ in the water channel using a K-type surface-mounted, thin foil thermocouple attached to the water side of the foil heater. While systematically varying the foil heating in a quiescent environment, the mean temperatures were determined using the thermocouple and the corresponding constant liquid crystal color was photographically captured and digitally analyzed; 24 hue–temperature pairs were established, spanning the color range of the liquid crystals from red to blue. The hue component (averaged over a 0.25-cm^2 area around the thermocouple contact) and the corresponding temperature were used to construct the hue versus-temperature-calibration curve.

Utilizing "Spyglass" data visualization software and the hue–temperature calibration curve, the 2-D hue pixal arrays were converted to comparable temperature arrays, representing the instantaneous spatial surface temperature. Because heat flux and free-stream temperature remain constant during a test sequence, the derived temperature arrays can be employed to establish instantaneous spatial arrays of heat transfer coefficient and Stanton number over the observed surface directly. These spatial arrays can then be used to establish mean, fluctuating, and temporal surface heat transfer behavior.

The uncertainties in the fluid properties, liquid crystal indications, temperature measurements, and heat flux settings combined to give an uncertainty range of 5 to 15% over the activation range of the liquid crystals. A typical free-stream temperature was 23°C, while the activation range of the LC was 25 to 30°C. The two major contributing factors to the uncertainty were the applied heat flux and the surface temperature field determined from the liquid crystal images.

Results

Flow visualization

Detailed hydrogen bubble flow visualization of the junction region of the rectangular block illustrated the presence of a dominant, resident horseshoe vortex, as detected in previous studies (Devenport and Simpson 1990; Pierce and Shin 1992), as well as the intermittent development of other ancillary vortices. By varying the location of the bubble wire, thus the introduction of the visualizing bubbles, the behavior of both the resident horseshoe vortex and the other developing vortices were visualized and examined in detail. In general, the horseshoe vortex moves erratically (both vertically and horizontally) within a fixed range from the block; on the symmetry plane, the horseshoe vortex resides, on the average, at $x/W \approx -0.3$ (where W is the width of the block) and $y/W \approx 0.8$. As illustrated in Figure 1, vortices of opposite- sign rotation to the horseshoe vortex are observed to form intermittently on the upstream side of the horseshoe vortex. Upon generation, these secondary vortices display a contiguous structure, stretching around the block in conjunction with and in proximity to the horseshoe vortex. In addition, a small corner vortex of negative rotation seems to remain resident in the very near corner of the junction at $x/W \approx -0.05$.

An example of the origin of the secondary vortices is illustrated in Figure 5, which is a particle visualization centered at $x/W \approx -0.32$ on the symmetry plane. As a horseshoe vortex (HV) comes into proximity of the surface, a secondary vortex (SV) is generated (Figure 5a). As time passes, a focusing of the surface fluid between the HV and the SV develops (Figure 5b), followed by consequent ejection of the SV from the surface and an eruption of the surface fluid (Figure 5c, d). Note that the vortex–surface interaction process illustrated in Figure 5 is essentially that suggested by previous numeric simulations (Walker 1978; Peridier et al. 1991), as illustrated previously in Figure 2. Once ejected, these SVs were observed to interact with the HV, inducing motion of the HV away from the surface. However, subsequent vortices (and vorticity) from the impinging turbulent boundary layer also interact with the HV, generally creating an induction of the HV back toward the surface, where the generation of subsequent SVs will occur. Thus, the resultant interaction of both the impinging boundary-layer vortices and the SVs with the horseshoe vortex creates an erratic vortex induction process that appears responsible for the resultant unsteadiness of the horseshoe vortex.

Vorticity contours

Using the PIV procedure described above, isovorticity contours were established for a sequence of 60 particle images. An assessment of the contours indicates consistency with the flow visualization observations in regard to the generation of SVs attributable to surface interaction of the HV. From an examination of the PIV images, the center of HV was determined to move within an envelope bounded by $-0.21 < x/W < -0.35$ and $0.043 < y/W < 0.128$. A typical sequence of isovorticity contours is shown in Figure 6, which spans a 1.5-s interval or $\Delta t U/W = 1$. In this figure, the horseshoe vortex is the series of concentric dotted (positive vorticity) contours appearing at $x/W \approx -0.3$. In the first vorticity field, at $t = 0$ s, the HV is just beginning its interaction with the surface, with a SV of negative vorticity starting to form at $x/W \approx -0.4$ and $y/W \approx 0.03$. By $t = 0.5$ s, the HV has moved slightly downward and upstream, causing the SV to begin to lift away from the plate, so that by $t = 1.0$ s, the SV is being ejected from the surface fluid. The ejection process is complete by $t = 1.5$ s, with the original negative vorticity surface fluid having been ejected into the outer region, where it subsequently cross-diffuses with the vorticity of the HV. Note the

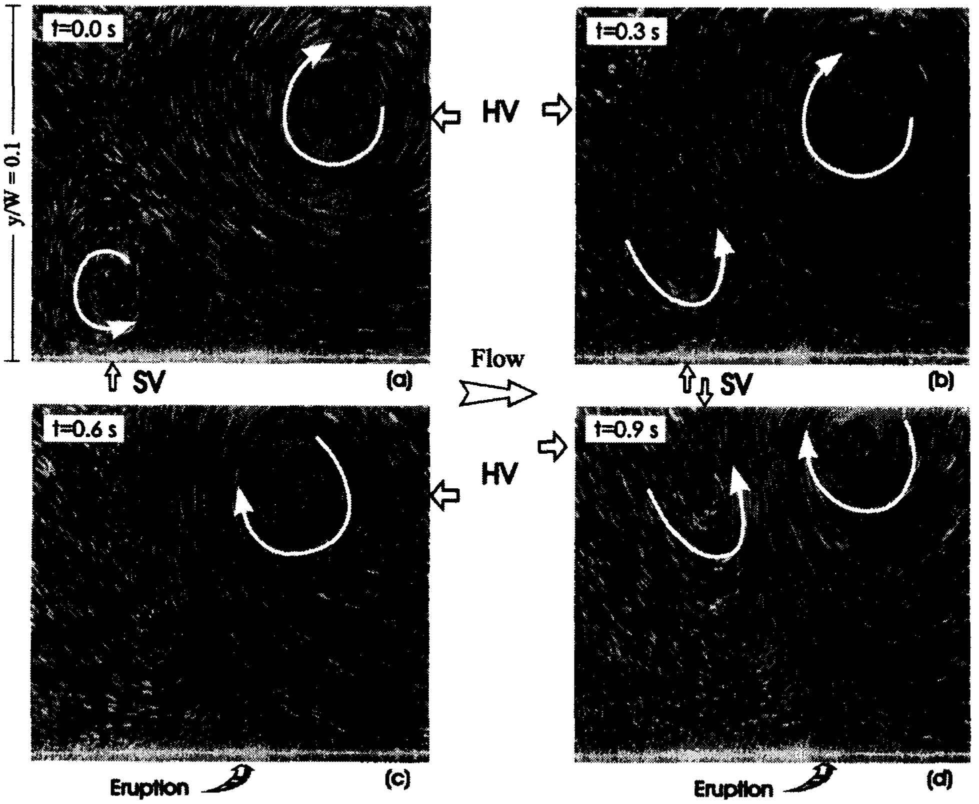

Figure 5 Temporal particle visualizations of a turbulent horseshoe vortex

remarkable similarity of the observed behavior to the vortex–surface interaction behavior originally proposed by Walker (1978), as well as the sporadic nature of this ejection process as compared to the behavior with a laminar approach flow, as illustrated in Figure 3.

Heat transfer results

A flat-plate base case without a bluff body was established for the impinging turbulent boundary layer using 11 liquid crystal images taken over a 2-s period with a constant surface heat flux of 4255 W/m^2. Figure 7a is a typical gray-scale presentation of local instantaneous Stanton number obtained after image processing and calibration. The image is clearly dominated by elongated streamwise regions, indicative of the characteristic high- and low-speed streaks in the near-wall region (Smith and Metzler 1983). Figure 7b, a probability distribution of the values comprising Figure 7a, suggests a strongly skewed distribution of a log-normal shape, similar to the types of distributions noted previously for low-speed streak-spacing (Smith and Metzler), with a range in Stanton number of 2.50×10^{-3} to 1.25×10^{-3}. The

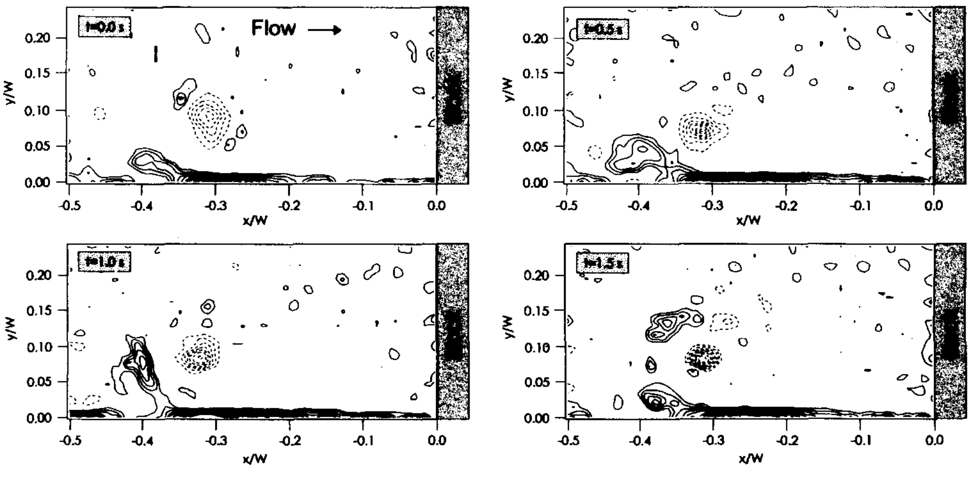

Figure 6 Temporal vorticity contour sequence obtained by means of PIV; dashed lines indicate positive vorticity (ranging from -95 to -15 in intervals of 10 s^{-1}); solid lines indicate negative vorticity (ranging from 5 to 50 intervals of 5 s^{-1})

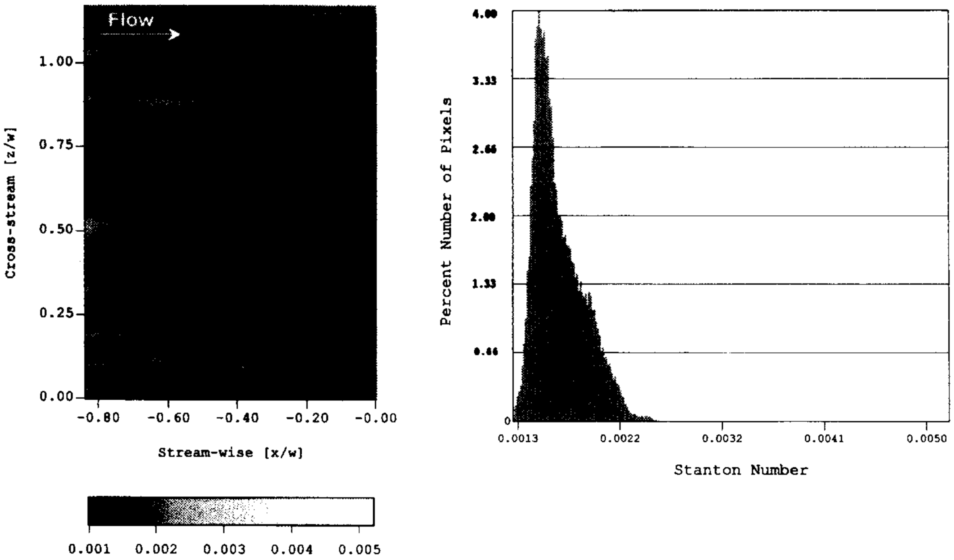

a) Instantaneous Stanton number for flat-plate turbulent boundary layer.

b) Stanton number probability distribution for flat-plate flow.

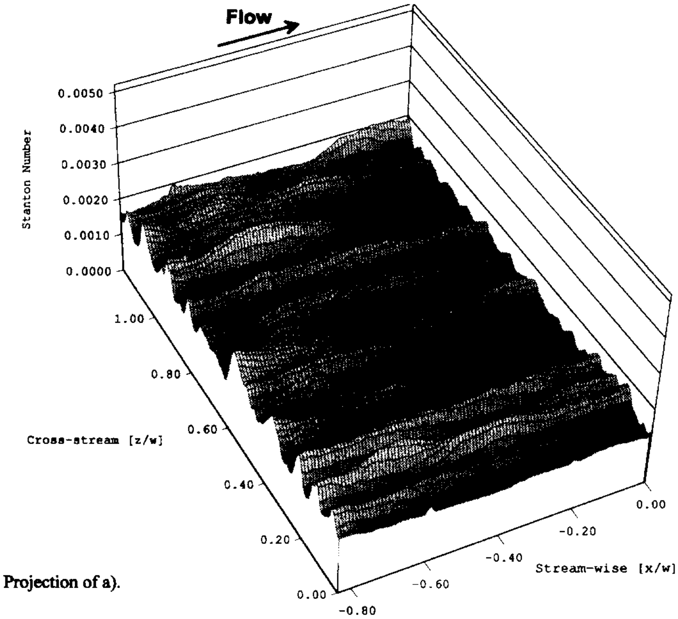

c) Projection of a).

Figure 7 Instantaneous Stanton number for a flat-plate turbulent boundary layer flow: a) gray-scale image; b) Stanton number probability distribution; c) projection of a); $U = 10$ cms/s, $q'' = 4255$ W/m^2, $T_\infty = 23.25$°C, Re ≈ 600

spatial–temporal average Stanton number over the 11 images is 1.67×10^{-3}, which is approximately 3% greater than the average value calculated using an empirical relation for a constant heat flux surface with unheated starting length (Kays and Crawford 1980). ($\mathrm{ST}_x = 0.030\,\mathrm{Re}_x^{-0.2}\mathrm{Pr}^{-0.4}[1 - \xi/x)^{0.9-0.111}$, where x is location from the unheated leading edge, and ξ is the length from the initiation of heating.) The rms Stanton number for the 11 images is 3.05×10^{-4}, or about 18% of the average value. Figure 7c, a projection of Figure 7a, illustrates the pronounced transverse variation in Stanton number attributable to the streamwise "streaks." This pattern was observed to change relatively slowly over the 11 data images, as would be expected, because the time period covered by the images is approximately $t^+ = tu_\tau^2/\nu \approx 58$, or about half a typical turbulent bursting period. The average lateral spacing of the ridges in figure 7c is approximately $\lambda = 0.017$ m, or nondimensionally $\lambda^+ = \lambda u_\tau/\nu \approx 98$, which is consistent with the typical nondimensional low-speed streak spacing of 100[13], this consistency suggest that although this is a low-Reynolds number flow, it properly reflects accepted near-wall flow structure characteristics.

Figure 8 is one of 14-gray-scale Stanton number images (spanning 2.5 s) obtained for the junction flow created with the rectangular block on the flat pate at the same flow and heat-flux conditions is used for Figure 7. The most obvious differences between Figure 7 and 8 are a rapid metamorphosis from a streamwise-dominant Stanton number pattern to a transverse-dominant pattern and substantial increases in local Stanton numbers. Although the vestiges of a low-speed streak pattern are apparent in the upstream portion of Figures 8a and 8c, these impinging "streaks" are more widely spaced because of the effect of the strong adverse pressure gradient imposed by the bluff body on the near-wall region. Interestingly, despite the wider

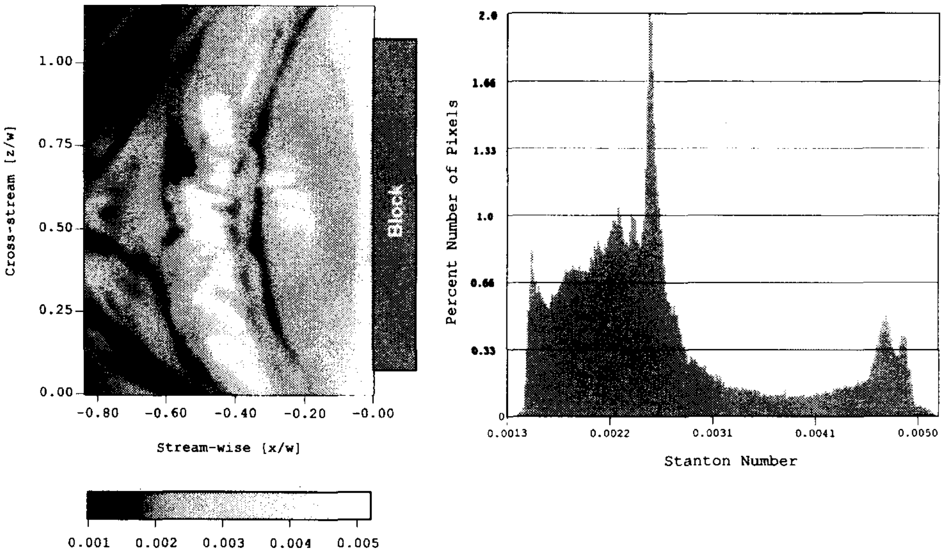

a) Instantaneous Stanton number in junction region.

b) Stanton number probability distribution for junction.

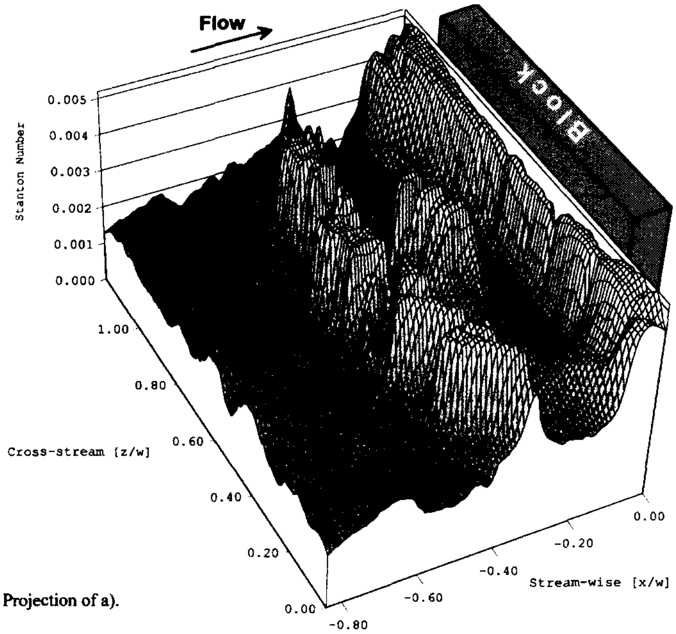

c) Projection of a).

Figure 8 Instantaneous Stanton number for a rectangular body turbulent junction flow at equivalent location as Figure 7; a) gray-scale image; b) Stanton number probability distribution; c) projection of a); $U_\infty = 10$ cm/s, $q'' = 4255$ W/m^2, $T_\infty = 23.35$°C

streak spacing, the spanwise-averaged Stanton number at $x/W = -0.84$ for both the junction region flow (Figure 8) and the conventional flat-plate boundary layer (Figure 7) are essentially identical (St $\approx 1.74 \times 10^{-3}$). However, as the turbulent boundary layer impinges on the bluff body, the streaks diverge laterally and are rapidly replaced by several transverse regions of sharply increased Stanton number.

The first region of increased Stanton number occurs near $x/W \approx -0.4$, appearing as a pronounced segmented ridge in Figure 8c, essentially mirroring the contour of the HV. On the symmetry plane, this first region develops approximately one-tenth of a block width upstream of the general location of the HV and is subject to substantial unsteady streamwise movement, in apparent coincidence with the unsteady behavior of the HV. Note that the ridge is not contiguous, but is comprised of a series of closely spaced regions of locally high Stanton number, often flanked by regions of much lower Stanton number; variances in Stanton number between these flanking regions were often in excess of 50%. The segmentation of this first region can be seen more clearly in Figure 9, which shows two other spatial Stanton number projections from the data sequence; this segmentation is particularly clear in Figure 9a. As a result of the unsteady behavior in this region, local pointwise excursions of up to 220% in Stanton number were observed across the 14 data images.

A second region of consistently elevated Stanton number is found very near the block between $x/W \approx 0$ and -0.08 and is characterized by the highest values of Stanton numbers observed for the data images. This is a relatively steady region, apparently

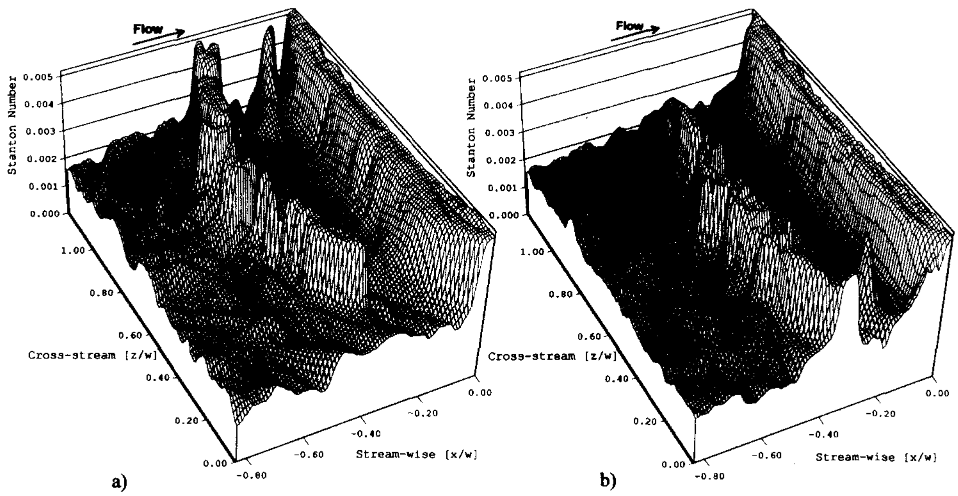

Figure 9 Projections of two instantaneous Stanton number images taken 2.5 s apart

dominated by a somewhat steady flow down the block toward the heat-flux surface. This downward flow originates from fluid a the edge of impinging boundary layer that first stagnates against the block, then moves toward the plate, and finally back upstream along the plate because of the block-induced adverse pressure gradient. The small near-corner vortex identified in the flow visualization studies appears to mediate the otherwise elevated Stanton number behavior very near the block by "trapping" a certain amount of fluid in the corner, which actually *lowers* the Stanton number in the very near corner of the junction. (This decrease is seen more clearly in symmetry-plane plots of Stanton number shown later in Figure 10.)

A third region of elevated temperature is reflected by somewhat isolated "peaks" in Stanton number that occur somewhat sporadically for $-0.10 < x/W < -0.30$. Examples of these peaks are evident in Figure 8c and are reflected by the local light region at $x/W \approx -0.22$ and $z/W \approx 0.60$ in the gray-scale image of Figure 8a. The projections of Figure 9 also reflect the presence and random development of these transient Stanton number peaks.

Finally, a characteristic region of *low* Stanton number, which again seems to mirror the shape of the HV, is noted for all 14 image dataframes. This region appears as the thin, dark region bowed out from the block at $x/W \approx -0.30$ in Figure 8a. This region seems to be consistent with the region indicated in the particle visualizations of Figure 5 as a focused region of eruptive fluid adjacent to the surface and is consistent with the results of previous computational studies (Puhak et al. 1993) that noted a local decrease in Stanton number caused by vortex-induced unsteady surface separations.

Figure 8b is the probability distribution of the Stanton number from Figure 8a, which reflects the marked variations in Stanton number over the junction region. The range in Stanton

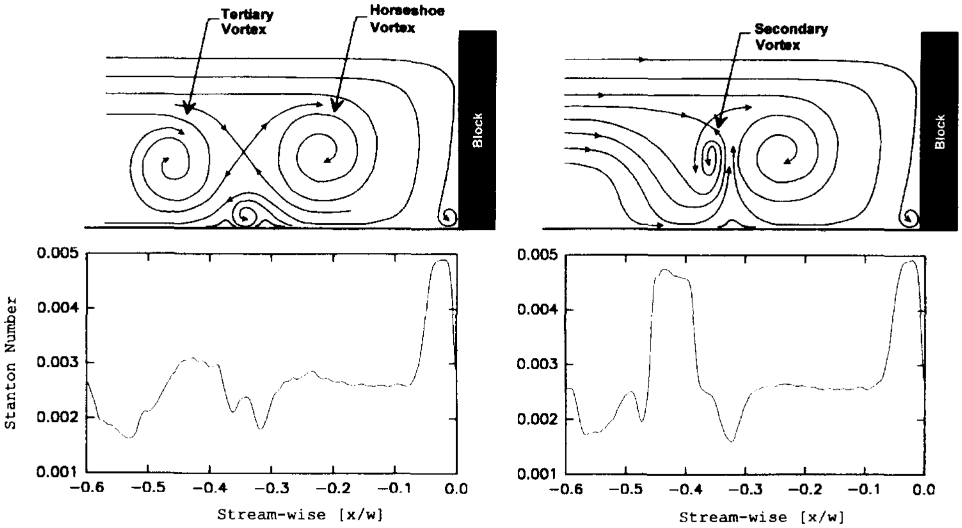

a) Secondary vortex formation

b) Ejection of SV with inrush of replacement fluid.

Figure 10 Streamline schematic models with corresponding prototypical instantaneous Stanton number distributions within the symmetry plane number from 5.0×10^{-3} to 1.4×10^{-3} indicates maximum excursions in Stanton number that are twice the maximum noted for the canonical turbulent boundary layer, and much more prevalent. The resultant spatial–temporal average Stanton number over the 14 images was 2.69×10^{-3}, attributable primarily to the elevated values of Stanton number within the discrete regions discussed above; this reflects a 62% increase over the average for the flat-plate flow under the same conditions. The skewed bimodal appearance of the probability distribution reflects the influence of the localized regions of high Stanton number.

Physical model

Collective evaluation of the visualization, PIV, and heat transfer results has allowed a synthesis of a physical model that correlates the observed vortex–surface interactions in the junction region with the localized, increased surface heat transfer. Figure 10 is a two-frame sequence representing the two most common types of vortex–surface interactions observed for the turbulent-junction flow. The four-votex model illustrated in Figure 10a matches the model proposed by Ishii and Honami (1986) from their experimental investigation of a turbulent juncture flow. Figures 10a and b each show actual streamwise, symmetry-plane Stanton number profiles (below), juxtaposed with simplified streamline patterns indicative of the hypothesized, instantaneous flow pattern (above). Note that in both these frames, the flow very near the block is depicted as relatively consistent and steady. As discussed above, this seems to be the result of a somewhat steady flow of fluid down the block from an outer region stagnation point, which creates a very elevated, but relatively steady-state Stanton number; the influence of the near-corner vortex on the observed Stanton number reduction very near the block is also depicted.

Figure 10a illustrates a characteristic pattern in which the HV is in the initial stages of interaction with the surface fluid, causing a focusing of surface fluid and the generation of a secondary, opposite rotation vortex. The presence of a tertiary vortex of the same rotation as the HV is illustrated immediately upstream of this interaction region. The presence of such a tertiary vortex was observed consistently during the early stages of HV interaction, although the tertiary vortex was of sporadic size and strength. This particular flow configuration did not immediately promote the exchange of surface fluid; so while surface heat transfer is elevated above that for a turbulent boundary layer, Stanton numbers near $x/W \approx -0.4$ are not particularly elevated.

Figure 10b illustrates a typical pattern representative of the completion of the HV interaction process. Here, the process of surface–vortex interaction has culminated in an eruption of surface fluid and the ejection of the secondary vortex into the outer region, reflective of the processes illustrated in Figures 2d, 5d, and 6d. As pointed out previously, the erupting surface fluid will be of high temperature, and thus reflective of a lower Stanton number, as illustrated by the valley in the profile at $x/W\_ - 0.32$. However, when the surface fluid erupts, the character of the upstream flow changes dramatically, with the tertiary vortex disappearing (the process by which this occurs is still under study) and being replaced by an inrush of outer region fluid. This strong inflow of cool fluid creates a strong peak in Stanton number, reflective of the high Stanton number ridge noted at $x/W\_ - 0.4$ in Figures 8 and 9. Following this inrush, the HV will strengthen and subsequently initiate another interaction process, as it moves irregularly back into proximity to the surface.

Thus, the repetitive and cyclical process of vortex interaction, surface fluid eruption, and inflow of outer region fluid creates the significantly increased, but temporally irregular heat transfer in the junction region. Note that while Figure 10 depicts this process two-dimensionally, the process is very spanwise irregular, in both time and space; thus, it is hypothesized that the processes depicted in Figures 10a and b occur in spanwise flanking regions, thus giving rise to the segmented appearance of the noted high-Stanton number ridge at $x/W \approx -0.4$ and probably the other isolated peaks in Stanton number nearer the block. It is the development of such vortex three-dimensionality, and the corresponding influence on the local surface heat transfer processes that is the subject of ongoing investigations of junction-region turbulent heat transfer.

References

Adrian, R. J. 1991. Particle-imaging techniques for experimental fluid mechanics. *Ann. Rev. Fluid Mech.*, **23**, 261–304

Devenport, W. J. and Simpson, R. L. 1990. Time-dependent and time averaged turbulence structure near the nose of a wing-body junction. *J. Fluid Mech.*, **210**, 23–55

Ersoy, S. and Walker, J. D. A. 1995. Viscous flow induced by counter-rotating vortices. *Phy. Fluids*, **28**, 2687–2698

Ireland, P. T., Jones, T. V. 1986. Detailed measurements of heat transfer on and around a pedestal in fully developed passage flow In *Proceedings of the 8th Int. Heat Transfer Conference*, Vol. 3, C. L. Tien et al. (eds.), Hemisphere, Bristol, PA, 795–980

Ishii, J. and Honami, S. 1986. A three-dimensional turbulent detached flow with a horseshoe vortex. *J. Gas Turbines Power*, **108**, 125–130

Kays, W. M. and Crawford, M. E. 1980. *Convective Heat and Mass Transfer*, 2nd ed., McGraw-Hill, New York, 216–217

Lewis, D. J., Simpson, R. L. and Diller, T. E. 1994. Time-resolved surface heat flux measurements in the wing/body junction vortex. *J. Thermophys. Heat Transfer*, **8**, 656–663

Ölcmen, S. M. and Simpson, R. L. 1994. Influence of wing shapes on the surface pressure fluctuations of a wing–body junction. *AIAA J.*, **32**, 6–15

Peridier, V. J., Smith, F. T. and Walker, J. D. A. 1991. Vortex-induced boundary layer separation. Part 1. The unsteady limit problem $\mathrm{Re} \to \_$. *J. Fluid Mech.*, **232**, 99–131

Pierce, F. J. and Shin, J. 1992. The development of a turbulent junction vortex system. *J. Fluids Eng.*, **114**, 559–565

Puhak, R., Degani, A. T. and Walker, J. D. A. 1993. Separation and heat transfer upstream of obstacles. In *Advances in Analytical Methods in Modeling of Aerodynamic Flows, Proceedings of the International Workshop on Advances in Analytical Methods in Modeling of Aerodynamic Flows*, (Miedzyzdroje, Poland), AIAA, New York

Rockwell, D., Magness, C., Towfighi, J., Akin, O. and Corcoran, T. 1993. High image-density particle image velocimetry using laser scanning techniques. *Exp. Fluids*, **14**, 233–270

Seal C. V., Smith C. R., Akin, O. and Rockwell, D. 1995. Quantitative characteristics of a laminar, unsteady necklace vortex system at a rectangular block-flat plate juncture. *J. Fluid Mech.*, **286**, 117–135

Smith, C. R. and Metzler, S. P. 1983. The characteristics of low-speed streaks in the near-wall region of a turbulent boundary layer. *J. Fluid Mech.*, **129**, 27–54

Walker, J. D. A. 1978. The boundary layer due to a rectilinear vertex. *Proc. R. Soc. Lond. A*, 359, 167–188